Small Molecule Inhibitors of the BfrB−Bfd Interaction Decrease *Pseudomonas aeruginosa* Fitness and Potentiate Fluoroquinolone Activity

Achala N. D. Punchi Hewage,[†,●] Huili Yao,[‡,●] Baskar Nammalwar,[§,▲] Krishna Kumar Gnanasekaran,[§,▲] Scott Lovell,[‖] Richard A. Bunce,[§] Kate Eshelman,[†,▲] Sahishna M. Phaniraj,[⊥] Molly M. Lee,[⊥,▲] Blake R. Peterson,[⊥] Kevin P. Battaile,[#] Allen B. Reitz,[¶] and Mario Rivera*,[‡]

[†]Department of Chemistry, University of Kansas, 2030 Becker Drive, Lawrence, Kansas 66047, United States

[‡]Department of Chemistry, Louisiana State University, 229A Choppin Hall, Baton Rouge, Louisiana 70803, United States

[§]Department of Chemistry, Oklahoma State University, Stillwater, Oklahoma 74078, United States

[‖]Protein Structure Laboratory, University of Kansas, 2034 Becker Drive, Lawrence, Kansas 66047, United States

[⊥]Department of Medicinal Chemistry, University of Kansas, 2034 Becker Drive, Lawrence, Kansas 66047, United States

[#]IMCA-CAT, Hauptman Woodward Medical Research Institute, 9700 South Cass Avenue, Building 435A, Argonne, Illinois 60439, United States

[¶]Fox Chase Chemical Diversity Center, Inc., 3805 Old Easton Road, Doylestown, Pennsylvania 18902, United States

Ⓢ *Supporting Information*

ABSTRACT: The iron storage protein bacterioferritin (BfrB) is central to bacterial iron homeostasis. The mobilization of iron from BfrB, which requires binding by a cognate ferredoxin (Bfd), is essential to the regulation of cytosolic iron levels in *P. aeruginosa*. This paper describes the structure-guided development of small molecule inhibitors of the BfrB−Bfd protein−protein interaction. The process was initiated by screening a fragment library and followed by obtaining the structure of a fragment hit bound to BfrB. The structural insights were used to develop a series of 4-(benzylamino)- and 4-((3-phenylpropyl)amino)-isoindoline-1,3-dione analogs that selectively bind BfrB at the Bfd binding site. Challenging *P. aeruginosa* cells with the 4-substituted isoindoline analogs revealed a dose-dependent growth phenotype. Further investigation determined that the analogs elicit a pyoverdin hyperproduction phenotype that is consistent with blockade of the BfrB−Bfd interaction and ensuing irreversible accumulation of iron in BfrB, with concomitant depletion of iron in the cytosol. The irreversible accumulation of iron in BfrB prompted by the 4-substituted isoindoline analogs was confirmed by visualization of BfrB-iron in *P. aeruginosa* cell lysates separated on native PAGE gels and stained for iron with Ferene S. Challenging *P. aeruginosa* cultures with a combination of commercial fluoroquinolone and our isoindoline analogs results in significantly lower cell survival relative to treatment with either antibiotic or analog alone. Collectively, these findings furnish proof of concept for the usefulness of small molecule probes designed to dysregulate bacterial iron homeostasis by targeting a protein−protein interaction pivotal for iron storage in the bacterial cell.
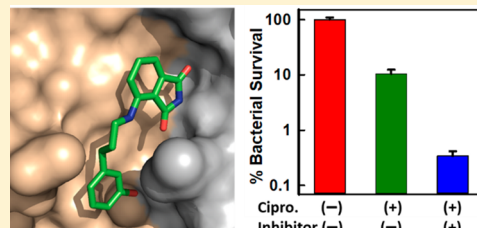
■ INTRODUCTION

Antibiotic resistant infections are a worldwide threat to public health. The challenge posed by the emergence of antibiotic resistant strains is compounded by slow to nearly stalled development of new antibiotics and validation of new targets.[1−3] Hence, antibiotic resistant infections have the potential to undermine many achievements in modern medicine, such as organ transplantation, major surgery, and cancer chemotherapy. The World Health Organization (WHO) published a priority list for research and development of new antibiotics to combat multidrug resistant bacteria, and assigned critical priority to the Gram-negative carbapenem-resistant *Acinetobacter baumanii* and *Pseudomonas aeruginosa*,

and third-generation cephalosporin resistant Enterobacteria-ceae.[4] *P. aeruginosa* is one of the leading Gram-negative pathogens associated with hospital infections due to their propensity to colonize urinary catheters and endotracheal tubes[5,6] and accelerate lung function decay that lowers the survival of cystic fibrosis patients.[7,8] Responding to this call requires vibrant research and continued investment in the early stages of drug development, in order to ensure a pipeline of novel ideas and approaches.[5] In this context, strategies that interfere with bacterial iron acquisition and homeostasis are
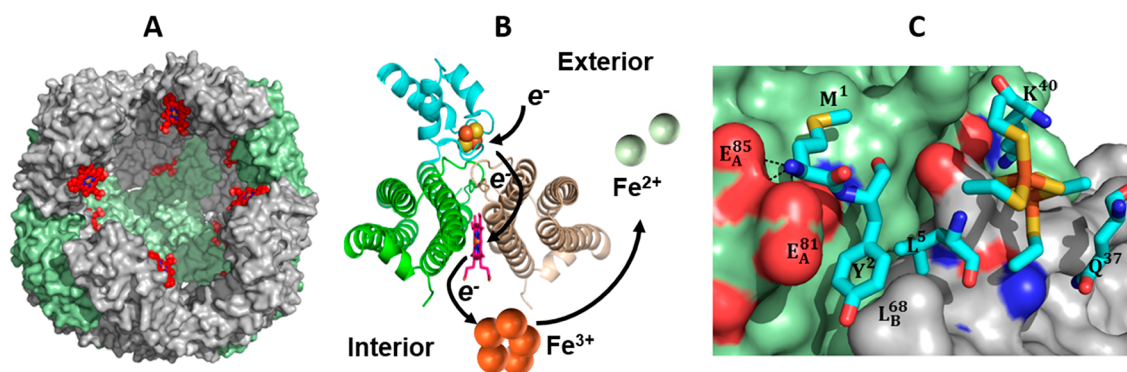
Figure 1. Structure and function of BfrB, Bfd, and the BfrB−Bfd complex. (A) BfrB is a nearly spherical molecule assembled from 24 identical subunits and 12 hemes. The 24-mer assembly harbors a hollow cavity approximately 80 Å in diameter where iron is stored in the form of a Fe^{3+} mineral. (B) Each heme molecule (red) is buried at the interface of a subunit dimer (green and gray), with the heme propionates protruding into the interior cavity. Each molecule of Bfd (cyan) binds BfrB at the subunit dimer interface to facilitate electron flow from the [2Fe−2S] cluster (orange and yellow spheres) in Bfd to the Fe^{3+} mineral in the interior cavity of BfrB through a heme, thus promoting the mobilization of Fe^{2+}. (C) Zoomed-in view of the BfrB−Bfd protein−protein interface, depicting the proximity of the [2Fe−2S] cluster in Bfd (orange and yellow) to the BfrB surface, as well as the burial of key Bfd residues (Y2 and L5) on pockets formed at the BfrB surface by residues L68 and E81.

regarded as having potential as new therapeutic interventions.[9−13] Iron is essential for bacteria because of its involvement in multiple metabolic processes, including respiration and fundamental enzymatic reactions.[14] Pathogenic bacteria must obtain iron from the host, but host nutritional immunity maintains extremely low concentrations of free iron, thus denying the essential nutrient to invading pathogens.[15−18] In addition, the very low solubility of the ferric ion (Fe^{3+}) severely limits its bioavailability, and the reactivity of the soluble ferrous iron (Fe^{2+}) toward hydrogen peroxide and oxygen induces oxidative stress. Consequently, the processes of bacterial iron homeostasis (acquisition, storage and utilization) are highly regulated to ensure sufficiency for metabolic needs while preventing iron-induced toxicity.[19,20] Herein, we describe a new approach to dysregulate iron homeostasis in *P. aeruginosa* that utilizes small molecule probes designed to block the interaction between the iron storage protein bacterioferritin B (BfrB) and its cognate partner, the bacterioferritin-associated ferredoxin (Bfd).

Bacteria store iron reserves in bacterial ferritin (Ftn) and in bacterioferritin (Bfr).[21−23] The roughly spherical and hollow structures of Bfr and bacterial Ftn, which are formed from 24 identical subunits, have an outer diameter of ~120 Å, an inner diameter of ~80 Å, and an interior cavity that can store up to ~3000 iron ions in the form of a Fe^{3+} mineral (Figure 1A). Bfrs, which exist only in bacteria, bind 12 heme groups buried under the external protein surface, with the heme propionates protruding into the interior cavity.[21,22] Despite sharing a nearly identical subunit fold and quaternary structures, the eukaryotic Ftns and the Bfrs share less than 20% sequence similarity, which results in divergent subunit packing, 24-mer dynamics and function.[23−26] Although in *P. aeruginosa* the *ftnA* and *bfrB* genes encode a bacterial ferritin (FtnA) and a bacterioferritin (BfrB), respectively,[27,28] BfrB functions as the main iron storage protein.[19] Importantly, the mobilization of iron stored in BfrB requires specific interactions with Bfd.[19,23,29] A crystal structure of the BfrB−Bfd complex revealed that up to 12 Bfd molecules can bind at identical sites on the BfrB surface, at the interface of subunit dimers, above a heme molecule (Figure 1B).[30] Characterization of the complex in solution showed that the 12 Bfd binding sites are equivalent and independent, and that Bfd binds to BfrB with a K_d of approximately 3 μM.[31]

These investigations also revealed that M1, Y2, and L5 in Bfd form a continuous set of interactions with L68 and E81 in BfrB, which contribute significantly to the stabilization of the BfrB−Bfd complex (Figure 1C). In agreement, the K_d values for the association between Bfd and the L68A or E81A mutants of BfrB are approximately 100-fold larger, and the association between Bfd and the BfrB L68A/E81A double mutant is undetectable.[31]

The repercussions of blocking the BfrB−Bfd interaction on *P. aeruginosa* iron metabolism have been investigated by deleting the *bfd* gene. These investigations, which showed an irreversible accumulation of Fe^{3+} in BfrB with concomitant iron deprivation in the cytosol, established the BfrB−Bfd interaction as a novel target to rationally induce iron homeostasis dysregulation in bacteria.[19] Consequently, it is important to discover small molecule inhibitors of the BfrB−Bfd interaction, which can be used as chemical probes to study bacterial iron homeostasis and uncover additional vulnerabilities in the bacterial cell exposed by iron metabolism dysregulation. Chemical probes are a powerful complement to the utilization of genetic techniques because they offer dose-dependent, selective, and temporal control over target proteins, which can be utilized in combination with other synergistic or antagonistic probes.[32,33] Herein we present the results from a structure-guided program aimed at the development of small molecules designed to inhibit the BfrB−Bfd interaction in *P. aeruginosa*. These novel probes are capable of penetrating the bacterial cells, where they inhibit the mobilization of iron from BfrB and elicit perturbations in iron homeostasis that decrease bacterial fitness, and also potentiate the bactericidal activity of fluoroquinolone antibiotics.

■ EXPERIMENTAL SECTION

Chemicals, Strains, and Growth Media. Chemicals were purchased from Fisher Scientific unless otherwise stated. *Pseudomonas aeruginosa* (PAO1) was purchased from the University of Washington Genome Center. The PAO1-derived strain with an unmarked, in-frame deletion of the *bfrB* gene had been prepared previously.[19] *P. aeruginosa* clinical isolates (MR3B and MR60) were obtained from Seattle Children's Research Foundation. [The clinical isolates of *P. aeruginosa* (strains isolated from the lungs of people with cystic fibrosis) were obtained from Seattle Children's Research Institute via the Antimicrobial Tools and Resources (Microbial Resources)

services offered by the Cystic Fibrosis Foundation (https://www.cff. org/Research/Researcher-Resources/Tools-and-Resources/Antimicrobial-Tools-and-Resources/).] All strains were kept on Pseudomonas Isolation Agar (PIA) (BD Biosciences, CA). M63 media was prepared as previously reported,[34] with a small modification. It contained per liter the following: 2 g of $(NH_4)_2SO_4$, 13.6 g of KH_2PO_4 (Sigma-Aldrich), 2 g of glucose, 4 g of citric acid, 0.25 g of tryptophan (Acros organics), 5 g of nontechnical grade casamino acids (BD scientific), and 0.24 g of $MgSO_4$ (Alfa Aesar), and the pH was adjusted to 7.0 with KOH. The M63 media also contained 0.1% (w/v) of hypermellose (HPMC, Sigma-Aldrich) to prevent aggregation of the analogs in aqueous solution.[35] Colorimetric analysis showed that the M63 media contains 2 μM Fe. When necessary, the M63 media was supplemented with additional iron by addition of a small volume of 1 mM $(NH_4)_2Fe(SO_4)_2$ (pH $\approx$ 2.0) to give the desired final iron concentration.

Fragment Library Screening Using Saturation Transfer Difference (STD) NMR Spectroscopy. Experimental details are presented in the Supporting Information.

Synthesis and Preparation of Analogs. Experimental details of the synthetic procedures developed to prepare compounds to be tested as inhibitors of the BfrB−Bfd interaction, as well as the corresponding ^1H and ^{13}C NMR spectra, are presented in the Supporting Information.

Crystallization, Ligand Soaking, and Data Collection. Crystallization screening was conducted in Compact 300 (Rigaku Reagents) sitting drop vapor diffusion plates at 18 °C using equal volumes (0.5 μL) of BfrB and crystallization solution equilibrated against 75 μL of the latter. Three different BfrB constructs were investigated to grow crystals of BfrB suitable for soaking experiments with the different fragments and analogs. BfrB crystals were observed in 1−2 days as follows: C89S/K96C BfrB: Red prismatic crystals were obtained from Wizard 1−2 (Rigaku Reagents) condition E2 (35% (v/v) 2-methyl-2,4-pentanediol, 100 mM MES 6.5, 200 mM Li_2SO_4). Apo-BfrB (BfrB devoid of heme): Colorless prismatic, or light yellow, crystals were obtained from the Wizard 3−4 screen (Rigaku Reagents) condition B1 (8% (w/v) PEG 8000, 100 mM Na acetate pH 4.6). BfrB: Red plates grew from the Cryo 1−2 HT screen (Rigaku Reagents) condition H6 (30% (v/v) PEG 200, 100 mM Na acetate pH 4.5, 100 mM NaCl). To prepare for soaking experiments, a stock solution (100 mM in DMSO) of each fragment or analog (compound) was mixed with crystallization solution to obtain a 20 mM compound solution to be used in soaking experiments. Crystals were transferred to these soaking solutions and incubated for 3.0 to 3.5 h before harvesting directly from the drop and storing in liquid nitrogen. Analog **13** was soaked in a 25 mM compound solution for 2 h, and analog **16** was soaked in a 10 mM compound solution for 3 h. The compound soaking solutions, which also served as the cryoprotectant, contained 80% crystallization solution and 20% DMSO. Structures of compounds bound to BfrB were obtained from the following compound/BfrB crystal combinations: Fragment **1**/C89S/K96C BfrB, analog **12**/apo-BfrB, and analogs **11**, **13**, **14**, **15**, **16**/BfrB. X-ray diffraction data were collected at the Advanced Photon Source beamline 17-ID using a Dectris Pilatus 6 M pixel array detector.

Structure Solution and Refinement. Intensities were integrated using XDS,[36] via Autoproc,[37] and the Laue class analysis and data scaling were performed with Aimless.[38] Structure solution was conducted by molecular replacement with Phaser,[39] and structure refinement and manual model building were performed with Phenix[40] and Coot,[41] respectively. Electron density omit maps for the ligands were calculated using the Polder omit routine[42] with the Phenix software suite. Structure validation was carried out with Molprobity,[43] and figures were prepared with CCP4mg.[44] The search models used for molecular replacement were as follows: C89S/K96C BfrB (PDB: 4TOF)[26] and BfrB (PDB: 5D8O).[31] Apo-BfrB: Structure solution was carried out using a single subunit of a previously determined structure of BfrB as the search model (PDB: 3IS7).[28] The top solution was obtained in the space group $C222_1$ with 12 molecules in the asymmetric unit.

Growth Curves and IC$_{50}$ Determination. Precultures (5 mL LB media) were grown for 12 h at 37 °C and 220 rpm in 50 mL conical tubes (VWR International, PA) covered with an air permeable membrane. The cells were then centrifuged at 4000 rpm for 10 min, and the resultant cell pellets were washed twice in M63 media and then diluted in M63 media to OD_{600} = 0.01. Stock solutions (100 mM) of analog in DMSO were prepared weekly and stored at 4 °C. Prior to initiating experiments in 96 well plates, the analog stock solution was serially diluted to make 10 mM or 1 mM working solutions in DMSO. A small volume of the appropriate working solution was transferred to a glass vial, diluted with DMSO to 30 μL, and then diluted to a final volume of 1.5 mL with preculture cell suspension with an OD_{600} = 0.01. The resultant cell suspension (200 μL) was transferred to a clear-bottom polystyrene 96 well plate (VWR) and incubated at 35 °C and 205 cpm for 13 h in an Epoch 2 microplate spectrophotometer (Biotek Instruments, Inc., Vermont). The growth curve in the presence of Ciprofloxacin was obtained in the same plate. To this end, 11.2 μL of a Ciprofloxacin working solution (100 μg/mL) were mixed with 30 μL of DMSO prior to diluting to a final volume of 1.5 mL with cell suspension having an OD_{600} = 0.01 and transferring to the plate. The resultant concentration of ciprofloxacin in the wells was 0.75 μg/mL, which is equivalent to 3 times the reported MIC.[45] Each condition was replicated in 5 wells of the plate, so the growth curves shown in Figures 5 and S5 are constructed from the average and standard deviation of 5 replicates. The growth % was estimated using the OD_{600} values obtained 13 h postinoculation and eq 1, where OD_T is the optical density of the culture treated with analog, OD_U is the optical density of the untreated control, and OD_{Cip} is the optical density of the culture treated with ciprofloxacin. To calculate the IC$_{50}$ values, the growth % was plotted as a function of log[analog (μM)] and fitted to eq 2, where the terms are defined as above and b is the slope factor.[46]

$$\text{growth \%} = \frac{(OD_T - OD_{Cip})}{(OD_U - OD_{Cip})} \times 100 \tag{1}$$

$$\text{growth \%} = OD_{Cip} + \frac{OD_U - OD_{Cip}}{1 + \left(\frac{\log[\text{analog}(\mu M)]}{IC_{50}}\right)^{-b}} \tag{2}$$

Analysis of Secreted Pyoverdin. These experiments were carried out in 96 well plates, as described above. *P. aeruginosa* cells treated with analog **11** or **16** (125 μM final concentration) were cultured for 13 h before the contents of each well were serially diluted in phosphate buffered saline (PBS, pH 7.4) and then plated on PIA plates to enumerate viable cells. The 500-fold diluted solution was centrifuged, and the cell-free supernatant was analyzed for pyoverdin by fluorescence spectrophotometry in a Synergy H1 microplate reader (Bioteck) with excitation at 400 nm and emission at λ_{max} = 455 nm. Full emission spectra (430−550 nm) were also recorded using a PerkinElmer LS50B spectrophotometer.

Imaging of Iron Stored in BfrB and Analysis of Total Iron Levels. Precultures were grown as described above, and cells were diluted in M63 media supplemented with 4 μM Fe (6 μM total Fe) to OD_{600} = 0.1 in 50 mL conical tubes. The resultant cell suspensions (5 mL) were mixed with a small volume of a 10 mM working solution of analog **16** in DMSO to give a 125 μM solution and 2% DMSO, or simply 2% DMSO (control). The conical tubes were covered with an air permeable membrane, and the cultures were incubated at 35 °C and 120 rpm for 6, 9, 12, 15, 18, 21, and 24 h. Prior to separating the cells by centrifugation (4000 rpm, 15 min), a 100 μL aliquot was withdrawn from each conical tube and serially diluted for plating and enumerating viable cells. The separated pellet was washed with 5 mL of PBS and frozen at −20 °C for subsequent analysis. The cell pellets were used to image iron stored in BfrB according to a previously described method[19] with some minor modifications. Briefly, cell pellets were suspended in 300 μL of lysis buffer (50 mM Tris pH 8.0, 20% glycerol, 20 mg/mL lysozyme, 0.2 mg/mL DNase, 100 mM NaCl, 10 mM $MgCl_2$, and 1% Triton X) and freeze−thawed twice

using liquid N_2. The resultant suspensions were incubated at 25 °C for 90 min in a rocker and then centrifuged at 12 500 rpm for 15 min at 4 °C. Lysate solutions (100 μL) were each mixed with 10 μL of the loading dye, and the samples (100 μL) were loaded onto a 3-mm-thick native polyacrylamide gel (8% resolving gel and 4% stacking gel) for separation. Electrophoretic separation was carried out at 60 V for 7 h at 4 °C, and the gels were stained with Ferene S[47] for 10 min in a solution containing 0.049 g of Ferene S, 250 μL of thioglycolic acid, 2.5 mL of acetic acid, and 100 mL of water. The scanned images were processed and compared using ImageJ.[48]

To determine the total iron levels of cells treated with analog **16** or DMSO only (control), 5 mL cultures were grown in M63 media supplemented with 4 μM iron, as described above, and analyzed at 12, 15, 21, 24, and 28 h. Prior to separation of the cells by centrifugation (4000 rpm, 15 min), a 100 μL aliquot was withdrawn from each conical tube and serially diluted for plating, in order to enumerate viable cells. Cell pellets were washed twice with 10 mL of PBS, and the total levels of cellular iron were measured using a published protocol.[19,49] In brief, cell pellets were mixed with 500 μL of freshly prepared digestion reagent (1:1 v/v 1.2 N HCl and 4.5% w/v $KMnO_4$ in water), thoroughly mixed by vortexing, and incubated at 65 °C for 4 h. The digested solutions were cooled to 25 °C, mixed with 500 μL of iron chelating agent (6.5 mM Ferene S, 13.1 mM neocuproine, 2 M ascorbic acid, 5 M ammonium acetate), and then incubated at 25 °C for 30 min. The iron concentration of the resultant solution was measured from the absorbance of the Fe^{2+}−Ferene S complex at 593 nm ($\varepsilon = 34{,}500$ M^{-1} cm^{-1})[50] using a Cary 60 UV−vis spectrophotometer, normalized by cell count and reported as Fe atoms per CFU (colony forming unit). The colorimetric determination of total intracellular iron offers a sensitive, accurate, and low cost analytical technique, which has been shown to produce results similar to those obtained by atomic inductively coupled plasma-mass spectrometry.[51]

Effect of Analogs on the Potency of Fluoroquinolone Antibiotics. Cultures were treated with (*i*) analog **16** only; (*ii*) ciprofloxacin (0.25 μg/mL), levofloxacin (0.5 μg/mL), or norfloxacin (0.9 μg/mL) only; and (*iii*) both fluorquinolone (concentration as above) and analog **16**. Precultures were grown as described above; the cells were then diluted in M63 media supplemented with 4 μM Fe to $OD_{600} = 0.1$ in 50 mL conical tubes. The resultant cell suspensions (5 mL) were mixed with a small volume of a 10 mM working solution of analog **16** in DMSO to give the desired analog concentration (75, 100, or 125 μM) and 2% DMSO, or simply with DMSO (untreated control). The conical tubes were covered with an air permeable membrane, and the cultures were incubated for 18 h at 35 °C and 120 rpm. The resultant cultures were serially diluted in PBS and plated on PIA for enumeration of viable cells. To treat cells with ciprofloxacin only, the procedure was identical except that the cell suspensions (5 mL) were mixed with a small volume of ciprofloxacin working solution (100 μg/mL) to give the desired antibiotic concentration and 2% DMSO. The combined treatment was carried out similarly, ensuring that the final concentration of DMSO was 2%.

Measurement of Dissociation Constants (K_d). Experimental details are presented in the Supporting Information.
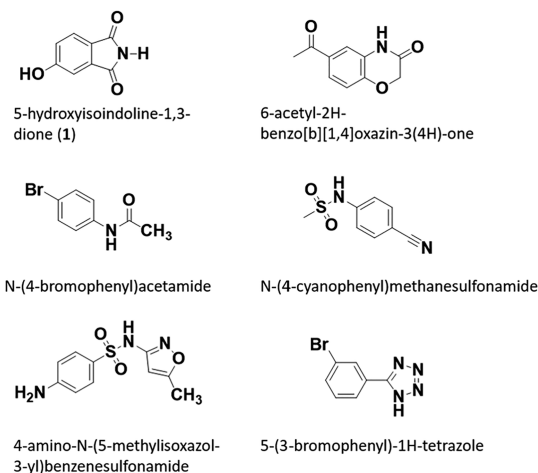
RESULTS

Screening and Detection of Fragment Binding to the Bfd Binding Site on BfrB. Structural information obtained from the BfrB−Bfd complex was used to design a fragment library to screen for molecules that bind BfrB at the Bfd-binding site. Bfd residues M1, Y2, and L5 and BfrB residues L68 and E81 dominate the buried surface area at the protein−protein interface (Figure 1C) and contribute significantly to the binding energy of the BfrB−Bfd complex.[31] Consequently, the fragment library was focused on fragments that may bind at the sites occupied by Y2 and L5 from Bfd and included groups with chemical properties similar to the aromatic and aliphatic side chains of Tyr and Leu, also utilizing standard fragment

criteria (MW < 300 Da, clogP < 3, and total count of hydrogen bond acceptors/donors <3 each). In addition, fragments capable of π−π stacking were included with both electron-rich and -deficient aromatic rings. To screen the library in search of fragments that bind BfrB at the Bfd-binding site we developed a competition assay that utilizes saturation transfer difference (STD) NMR spectroscopy. This technique is ideally suited to screen fragments that bind to the large BfrB (∼440 kDa) because protein resonance assignments are not necessary and very low protein concentrations are required. In addition, the large rotational correlation time (τ_c) of BfrB enhances spin diffusion and therefore saturation transfer within the protein and to the ligand.[52] Two solutions were prepared for each fragment: a solution of the fragment alone, and a solution of the fragment and BfrB. Three spectra were obtained for each fragment, as illustrated in Figure S1 of the Supporting Information for fragment **1**, which binds BfrB at the Bfd-binding site. The ^1H spectrum of the fragment alone was used to determine fragment integrity and solubility, the ^1H spectrum of the fragment in the presence of BfrB was used to corroborate that fragment integrity and solubility is not affected by BfrB, and the STD spectrum of the solution containing the fragment and BfrB was used to assess fragment binding. This strategy uncovered 18 compounds that bind BfrB. The specificity criterion for fragment binders, however, is that these bind BfrB specifically at the Bfd-binding site. To eliminate nonspecific binders, a displacement strategy was implemented that utilizes Bfd as a specific competitor. For this purpose, an STD spectrum was acquired from a solution containing fragment, BfrB and Bfd. Nearly complete disappearance of the STD signal indicates that the fragment binds BfrB at the Bfd-binding site. With the aid of this competitive displacement strategy, it was determined that of the 18 fragments that bind BfrB, the 6 molecules shown in Chart 1 bind at the Bfd-binding site. These fragments were advanced to the next stage, which was focused on uncovering structural information on fragment binding. Results from these experiments are presented below.

Structure-Based Optimization of Fragment Binders. A structure-guided approach was used to synthetically elaborate fragments discovered to bind BfrB at the Bfd-binding

Chart 1. Structures of Fragments Identified to Bind BfrB at the Bfd-Binding Site Using the Screening Strategy Described in the Text
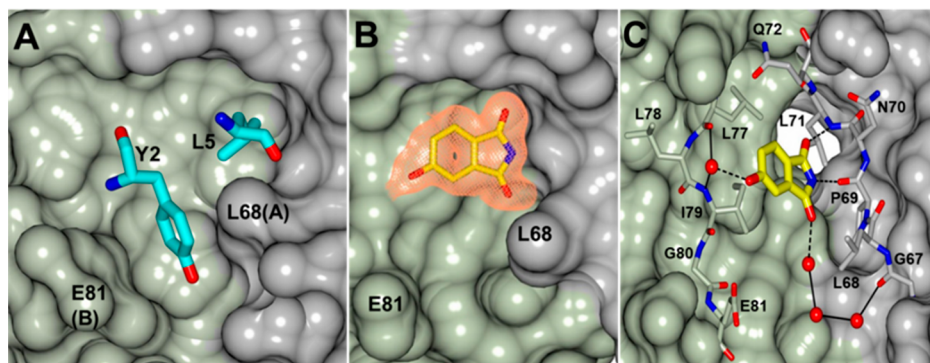

5-hydroxyisoindoline-1,3-dione (**1**)

6-acetyl-2H-benzo[b][1,4]oxazin-3(4H)-one

N-(4-bromophenyl)acetamide

N-(4-cyanophenyl)methanesulfonamide

4-amino-N-(5-methylisoxazol-3-yl)benzenesulfonamide

5-(3-bromophenyl)-1H-tetrazole

Figure 2. Protein−protein interaction interface of the BfrB−Bfd complex. Subunits A and B of a BfrB subunit dimer are colored gray and green, respectively. (A) Residues Y2 and L5 of Bfd (cyan cylinders) are positioned within pockets at the BfrB subunit dimer interface. (B) $F_o - F_c$ omit map (orange mesh) contoured at 3σ showing 5-hydroxyaminoisoindoline-1,3-dione (fragment **1**) bound within the cleft occupied by L5 in the BfrB−Bfd complex. (C) Hydrogen bond interactions (dashed lines) between fragment **1** and BfrB. Water mediated contacts are indicated by the solid lines.
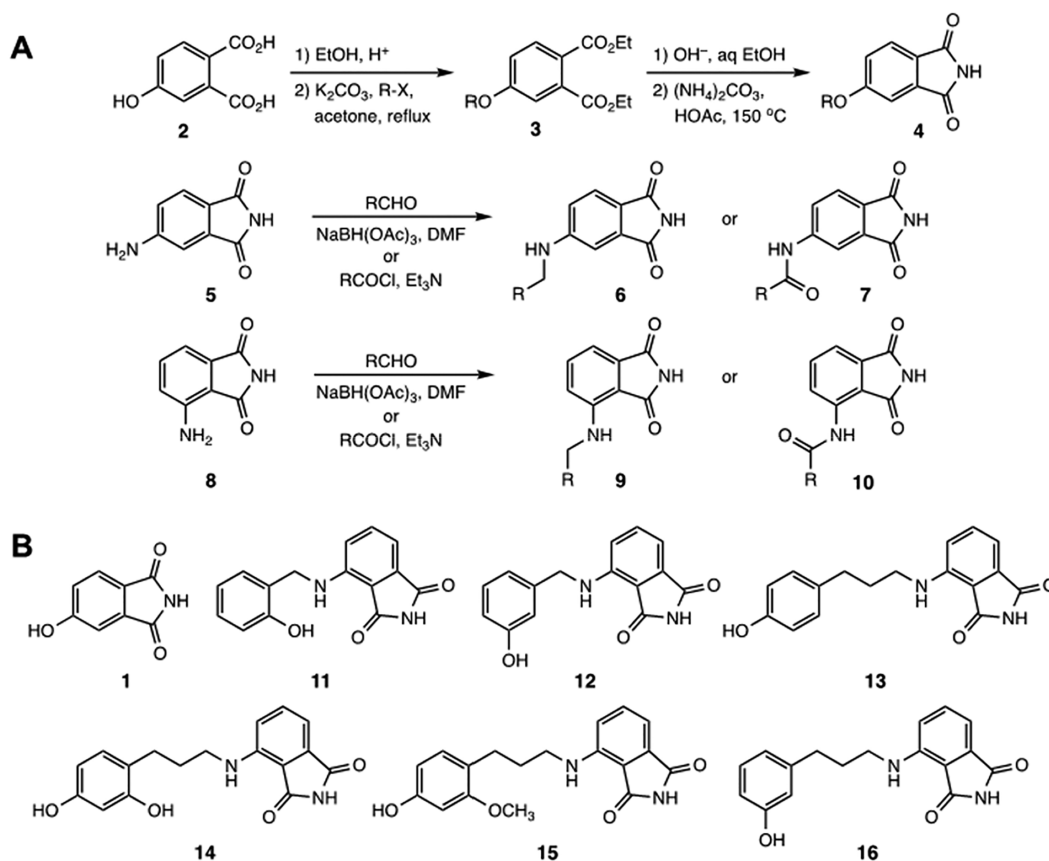

Figure 3. (A) Schematic summary of the synthetic procedures employed to prepare analogs of fragments **1**, **5**, and **8** to form ethers **4** derived from 5-hydroxyisoindoline-1,3-dione (**1**); amines **6** or amides **7** derived from 5-aminoisoindoline-1,3-dione (**5**); or amines **9** or amides **10** derived from 4-aminoisoindoline-1,3-dione (**8**). Descriptions of the synthetic procedures, as well as the characterization of the analogs are presented in the Supporting Information. (B) Structures of fragment **1** and analogs prepared from fragment **8**, which have been shown to bind BfrB at the Bfd binding site by X-ray crystallography.

site into analogs capable of binding with higher affinity. The affinity and selectivity of the fragments and analogs for the Bfd-binding site on BfrB were investigated by X-ray crystallography, surface plasmon resonance (SPR), and fluorescence polarization methods. The structures of fragments and derived analogs which have been demonstrated to bind BfrB at the Bfd-binding site using X-ray crystallography are shown in Figure 3B. During the course of these experiments, crystals

obtained from three different BfrB constructs were tested in ligand soaking experiments, in an effort to identify the "best" crystals for the study. Hence, crystals of BfrB (PDB 5D8O), C98S/K96C BfrB (PDB 4TOF), and apo-BfrB were soaked in crystallization solution containing the various analogs. The structure of 5-hydroxyisoindoline-1,3-dione (fragment **1**) bound to BfrB was obtained by soaking crystals of C98S/K96C BfrB in a solution of the fragment, as described in the

Experimental Section. In subsequent experiments, crystals of apo-BfrB were used because this protein formed robust, highly reproducible crystals. These experiments culminated in the structure of analog **12** bound to BfrB. It is important to underscore that the structure of apo-BfrB is nearly identical to that of BfrB, at the subunit level (RMSD = 0.18 Å), as well as the biological assembly level, including the Bfd-binding sites (Figure S2A). Additional evidence indicating that the Bfd-binding sites on apo-BfrB are unaffected relative to the holo-protein was obtained in the dissociation constant for the interaction between Bfd and apo-BfrB (K_d = 3.1 μM) (Figure S2B and C), which is nearly identical to that previously reported for the interaction between Bfd and holo-BfrB (K_d = 3.4 μM).[31,53] Finally, the BfrB protein also produced reproducible crystals that were isomorphs with those formed by apo-BfrB. Consequently, the structures of analogs **11** and **13−16** bound to BfrB were obtained by soaking crystals of BfrB in solutions of each of the analogs.

Figure 2A depicts a portion of the BfrB−Bfd complex interface and illustrates how Y2 and L5 in Bfd (cyan cylinders) contribute to anchor Bfd to the BfrB surface. A prior study indicated that interactions between L68 and E81 in BfrB and Y2 and L5 in Bfd contribute significantly to the binding energy of the BfrB−Bfd complex.[31] It was therefore surmised that fragments capable of binding to this region of the BfrB surface would be good candidates for subsequent structure-guided synthetic elaboration aimed at discovering inhibitors of the BfrB−Bfd interaction. To obtain the structures of fragments bound to BfrB, crystals of the protein were soaked in crystallization solution containing each of the 6 fragments found to bind BfrB at the Bfd-binding site with the aid of the competitive displacement STD NMR strategy described above. These efforts culminated in a 1.5 Å resolution cocrystal structure of 5-hydroxyisoindoline-1,3-dione (**1**) bound to BfrB (Figure 2B and 2C and Table S1), which showed that **1** binds BfrB at the Bfd-binding site, in the same pocket where L5 from Bfd would bind. The fragment rests on a platform at the base of a shallow depression on the BfrB surface formed by the side chains of L_B^{77} and I_B^{79} (the subscript denotes subunit, and the superscript denotes residue number), surrounded by a semicircular wall comprised by the side chain and backbone atoms of L_A^{68}, N_A^{70}, Q_A^{72}, and L_B^{77}. One of the carbonyl-oxygen atoms of **1** accepts a H-bond from the backbone NH of L_A^{71}, and its N−H group forms a H-bond to the backbone carbonyl of P_A^{69}. Additional stabilization for binding probably stems from the network of H-bonded waters linking a carbonyl oxygen in **1** and G_A^{67} in BfrB. This structural information suggested a strategy to grow **1**, or its analogs 4-aminoisoindoline-1,3-dione (**8**) and 5-aminoisoindoline-1,3-dione (**5**), by branching from the isoindoline ring carbons C4 or C5 to engage the cleft formed by the side chains of L68 and E81 in BfrB, where Y2 from Bfd anchors.

A general synthetic approach (Figure 3A) was formulated to generate a series of ether analogs represented by **4**, amine analogs represented by **6** or **9**, and amide analogs represented by **7** or **10**. Preparation of the ether analogs of **4** started with the esterification of the acid groups in 4-hydroxyphthalic acid **2**, followed by alkylation of the phenolic oxygen to produce **3** and subsequent base cleavage of the esters and cyclization to produce the isoindoline-1,3-dione ethers **4**. Synthesis of the amine analogs represented by **6** and **9** was carried out by reductive amination of **5** or **8**, respectively, with a series of aldehydes, whereas amide analogs **7** and **10** were obtained

from **5** or **8**, respectively, via reactions with a series of acid chlorides. The collection of ether, amine, and amide analogs prepared for this study, as well as the details of their synthetic preparation and characterization, are presented in the Supporting Information.

Although all of the compounds synthesized for each of the analog types shown in Figure 3A were tested in crystal soaking experiments, structures of analog-bound BfrB were obtained only for analogs **11−16** (Figure 3B), which are derivatives of 4-aminoisoindoline-1,3-dione (**8**) with −(CH$_2$)− and −(CH$_2$)$_3$− linkers. The pose of each of these analogs in the Bfd-binding site of BfrB is shown in Figures 4 and S3.
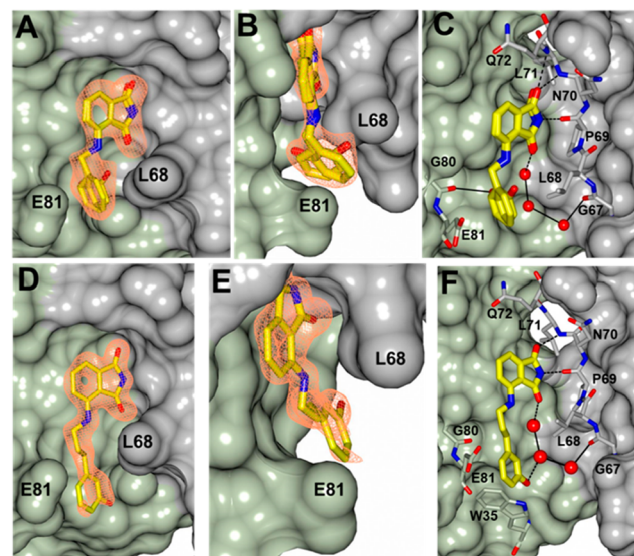

Figure 4. Binding modes of analogs **11** and **16** at the Bfd-binding site on BfrB. Subunits A and B of a BfrB subunit dimer are colored gray and green, respectively. (A) $F_o − F_c$ omit map (orange mesh) contoured at 3σ from analog **11** bound at the Bfd-binding site on BfrB. (B) Same as panel A but showing a different perspective to illustrate the two orientations modeled for the *o*-hydroxyphenyl ring of analog **11**. (C) Hydrogen bond interactions (dashed lines) between analog **11** and BfrB. Water mediated contacts are indicated by the solid lines. (D) $F_o − F_c$ omit map (orange mesh) contoured at 3σ from analog **16** bound at the Bfd-binding site on BfrB. (E) Same as panel D but rotated to illustrate the *m*-hydroxyphenyl ring of analog **16** positioned between the cleft formed by the side chains of L_A^{68} and E_B^{81} in BfrB. (F) Hydrogen bond interactions (dashed lines) between analog **16** and BfrB. Water mediated contacts are indicated by the solid lines.

Inspection reveals that the isoindoline-1,3-dione moiety in all the compounds invariably binds BfrB in a manner identical to that described above for fragment **1** binding to BfrB (see Figure 2). In addition, and as was expected, the benzyl portion of the analogs extends to engage the cleft formed by the side chains of L_A^{68} and E_B^{81} in BfrB via hydrophobic packing interactions. The interactions experienced by analog **11** at the Bfd-binding site on BfrB are illustrated in Figure 4A−C. Strong electron density consistent with the compound can be observed in 9 of the 12 subunits in the asymmetric unit; the 3 subunits in which compound **11** was not modeled displayed electron density not associated with the protein at the Bfd-binding site, but this electron density was too weak to model the ligand. The *o*-hydroxyphenyl ring of **11** is observed in two orientations that differ by a 180° rotation of the ring; one

Table 1. Structure, Binding Affinity, and IC$_{50}$ of 4-Aminoisoindoline-1,3-dione Derivatives

Analog	Structure	K_d (μM)	IC$_{50}$ (μM)
8	isoindoline-1,3-dione with 4-NH$_2$	300 ± 50	not active
11	N-(2-hydroxybenzyl)amino isoindoline-1,3-dione	11 ± 1	258 ± 23
12	N-(3-hydroxybenzyl)amino isoindoline-1,3-dione	15 ± 2	not active
13	4-hydroxyphenyl propyl amino isoindoline-1,3-dione	3 ± 1	201 ± 18
14	3,4-dihydroxyphenyl propyl amino isoindoline-1,3-dione	4 ± 2	143 ± 8
15	3-hydroxy-4-methoxyphenyl propyl amino isoindoline-1,3-dione	5 ± 2	227 ± 10
16	3-hydroxyphenyl propyl amino isoindoline-1,3-dione	6 ± 1	121 ± 4

orientation places the hydroxyl group pointing toward the base of the cleft, where it forms a hydrogen bond with G_B^{80}, while the second orientation places the hydroxyl group toward the solvent and enables packing of the *o*-hydroxyphenyl ring and the −(CH$_2$)− moiety bridging the phenyl and isonindoline rings against the side chains of M_B^{31} and I_B^{79}, respectively. Additional stabilization for binding probably stems from the network of H-bonded waters linking a carbonyl oxygen in **11** and G_A^{67}, similar to the network of H-bonded water molecules observed in the structure of **1** bound to BfrB (see Figure 2C). The structure of a similar analog (**12**) bound to BfrB shows identical interactions of the isoindoline-1,3-dione moiety with BfrB and similar interactions of the phenyl ring with the cleft formed by the side chains of L_A^{68} and E_B^{81} on the BfrB surface (Figure S3A−C).

A similar close view of compound **16** bound at the Bfd binding site on BfrB (Figure 4D−F) illustrates how the isoindoline-1,3-dione ring presents the same pose and set of interactions as those described above for fragment **1** and analogs **11** and **12**. Clear electron density consistent with the compound can be observed in all 12 subunits in the asymmetric unit, but the *m*-hydroxyphenyl ring was partially disordered in several of the subunits. The *m*-hydroxyphenyl ring and the −(CH$_2$)$_3$− linker pack against the L_A^{68} and hydrophobic portion of the E_B^{81} side chains, with additional stabilization probably stemming from a network of H-bonded

waters connecting a carbonyl oxygen in the isoindoline-1,3-dione ring, the hydroxyl group on aromatic ring, and the carbonyl oxygen in L_A^{68}. The structures of four additional compounds similar to **16** bound to BfrB (Figure S3), which show a nearly identical pose of the isoindoline-1,3-dione moieties and very similar interactions of the linkers and phenyl rings, demonstrate the specificity with which the series of 4-amino derivatives listed in Table 1 engage the Bfd-binding site on BfrB.

Prior to testing the effect that the 4-substituted isoindoline-1,3-dione derivatives might exert on *P. aeruginosa* cells, the strength of their interaction with BfrB was evaluated *in vitro* with a fluorescence polarization assay developed based on the intrinsic fluorescence of the isoindoline-1,3-dione moiety. Because initial fluorescence spectroscopic measurements revealed that the heme groups in BfrB interfere with the signal of the fluorescent ligand, we utilized apo-BfrB for these measurements, capitalizing on our earlier findings that the Bfd-binding sites in apo-BfrB are nearly identical to those in BfrB, and that the K_d for the interaction between apo-BfrB and Bfd is very similar to that measured for the interaction between BfrB and Bfd (see above and Figure S2). Hence, the K_d values were measured by titrating apo-BfrB into a fixed concentration of the appropriate fluorescent 4-aminoisondoline-1,3-dione ligand while analyzing fluorescence polarization and intensity near the emission λ_{max} (Figure S4). The K_d values (Table 1) show that

analogs **11−16** exhibit significantly higher affinity than fragment **8**, observations that are in agreement with the structural insights, which revealed that growing the fragments from the isoindoline ring carbon C4 make it possible to engage the cleft formed by the side chains of L68 and E81 in BfrB. The two derivatives with a −(CH$_2$)− linker exhibit binding affinities approximately 2- to 5-fold lower than derivatives with a −(CH$_2$)$_3$− linker, also in agreement with a relatively more efficient hydrophobic packing facilitated by the longer linker.

4-Aminoisoindoline-1,3-dione derivatives elicit a growth retardation phenotype in *P. aeruginosa* cells. The binding affinity and structural information indicate that most of the analogs in Table 1 bind BfrB at the Bfd binding site with a strength comparable to that of the BfrB−Bfd association ($K_d = 3\ \mu M$), therefore suggesting that these compounds may be capable of interfering with the BfrB−Bfd interaction in the *P. aeruginosa* cytosol. As will be described below, this idea was investigated, first by demonstrating that the analogs elicit a growth phenotype in *P. aeruginosa*, and then by showing that one of the most potent analogs inhibits the mobilization of iron from BfrB in the bacterial cytosol.

To investigate the effect of the analogs on cell growth, cultures of *P. aeruginosa* in M63 media were challenged with 4-aminoisoindoline-1,3-dione derivatives, and their growth was monitored in 96 well plates by following the OD$_{600}$. Figure 5A

and 5B illustrate the dose-dependent growth inhibition observed upon challenging the cultures with analogs **11** and **16**, respectively; the highest concentration of analog used was determined by its solubility in PBS buffer, 250 μM for analog **11**, and 125 μM for analog **16**. Growth curves from similar experiments conducted with the other analogs in Table 1 are shown in Figure S5. In order to facilitate a quantitative comparison of the effect exerted by the analogs on *P. aeruginosa* growth, IC$_{50}$ values were calculated. To this end, the growth inhibition caused by each of the analogs was compared to that of the untreated culture (100% growth) and to the growth in the presence of ciprofloxacin present at a concentration equivalent to 3 times the reported MIC (0% growth). Hence, the relative growth in the presence of a 4-aminoisoindoline-1,3-dione analog, measured 13 h post-inoculation, is defined by eq 1 (see Experimental Section). The IC$_{50}$ values, obtained from fitting the plots relating growth % and analog concentration to eq 2 (Figures 5C, 5D and S5), are listed in Table 1. Comparison of these values shows that analog **16** is the most efficacious at inhibiting cell growth, despite a very similar binding affinity for BfrB when compared to similar analogs such as **13**, **14**, and **15**. The reasons for the higher efficacy of analog **16** to inhibit cell growth are not yet evident, but it is possible to speculate that these may be related to their relative ability to penetrate the *P. aeruginosa* cell and/or their reactivity/stability in cell culture.

To obtain initial insights on the selectivity of the analogs for their intended target in *P. aeruginosa*, mutant cells with a deletion of the *bfrB* gene (Δ*bfrB*) were challenged with analog **11** or **16**. To this end, wild type and Δ*bfrB* cells were cultured in M63 media supplemented with 4 μM Fe, in the presence of different concentrations of analog. The effect of the analogs on cell growth was evaluated 15 h postinoculation by plating and enumerating viable cells and comparing the cell growth of each strain to the corresponding untreated control (Figure 6A and
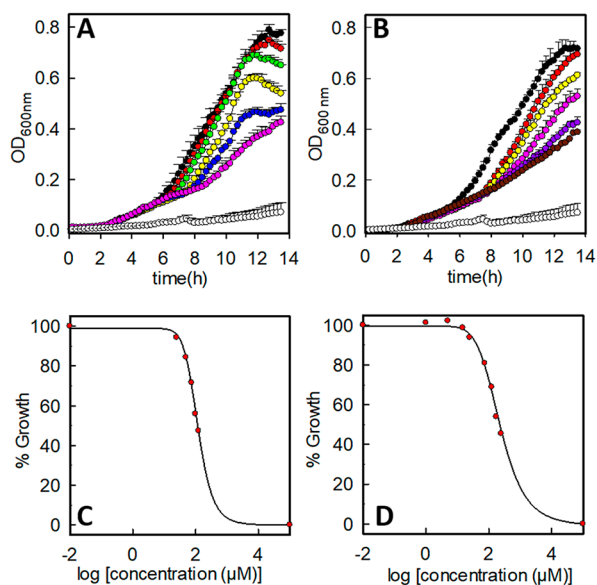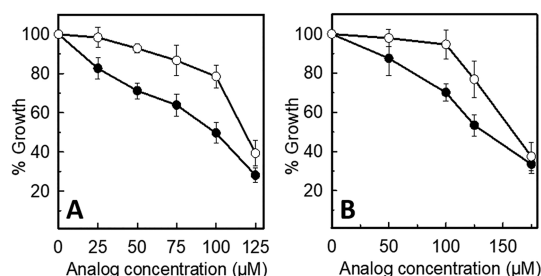

Figure 5. Analogs of 4-aminoisoindoline-1,3-dione elicit a growth defect in *P. aeruginosa*. Panels (A) and (B) show the time-dependent growth retardation of *P. aeruginosa* cultures treated with analogs **16** and **11**, respectively. The black circles correspond to untreated cells (DMSO control), and the open circles to cells treated with ciprofloxacin (0.75 μg/mL). The concentrations of analog **16** in (A) are 25 μM (red), 50 μM (green), 75 μM (yellow), 100 μM (blue), and 125 μM (magenta); the concentrations of analog **11** in (B) are 25 μM (red), 75 μM (yellow), 125 μM (magenta), 175 μM (purple), and 250 μM (brown). The corresponding IC$_{50}$ values (C and D) were obtained by calculating the % growth using OD$_{600}$ values at 13 h and fitting to eq 2, as indicated in the Experimental Section. Each of the growth curves was constructed from the average and standard deviation of 5 replicate wells. The IC$_{50}$ values (see Table 1) are the average and standard deviation from three independent experiments.

Figure 6. Deleting the *bfrB* gene (Δ*bfrB*) changes the monophasic dose-dependent growth response exhibited by the wild type *P. aeruginosa* cells to analogs **16** and **11** into a biphasic response, which is nearly independent of analog until ∼100 μM and rapidly toxic thereafter. The plots illustrate the growth % of the Δ*bfrB* (○) and wild type (●) cells relative to untreated control as a function of analog **16** (A) and analog **11** (B) concentration. The values at each point are the average and standard deviation from three independent experiments.

B). As expected, the analogs elicit a monophasic dose-dependent growth defect on the wild type cells. In comparison, the analogs induce a biphasic growth response on the Δ*bfrB* mutant cells, which consists of a shallow first phase (0−∼100 μM) that is nearly independent of analog concentration, followed by a steep second phase where the analogs become rapidly toxic. Since BfrB is not essential, it is likely that the cell
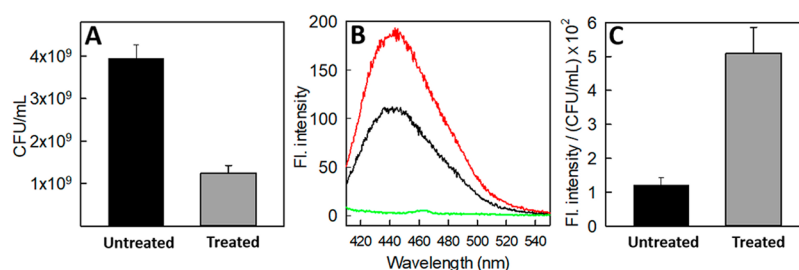
Figure 7. P. aeruginosa cells treated with analog **16** overproduce pyoverdin. (A) P. aeruginosa cultures treated with analog **16** (125 μM) for 13 h exhibit approximately 30% of the viable cells in the untreated DMSO control. (B) Fluorescence spectra obtained from cell free supernatants (13 h postinoculation) after a 500-fold dilution in PBS buffer, pH 7.4. The black trace is the spectrum from pyoverdin present in cell-free supernatant from untreated cells (DMSO control), and the red trace is the spectrum from pyoverdin in cell-free supernatant from samples treated with analog **16** (125 μM). The green trace was obtained after a 125 μM solution of analog **16** in M63 media was diluted 500-fold in PBS, to show that the relatively weak intrinsic fluorescence of the analog does not interfere with the strong fluorescence response from pyoverdin. (C) Fluorescence intensity normalized to the number of viable cells (CFU/mL) shows that cells treated with analog **16** secrete ~4.5-fold more pyoverdin than cells in the DMSO control. Error bars represent standard deviations from three independent experiments.
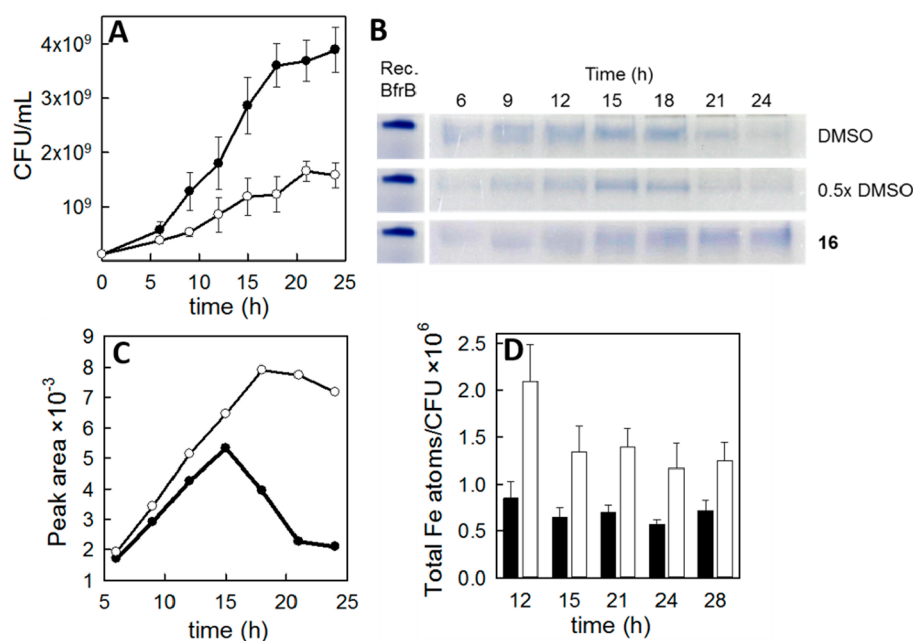

Figure 8. Analog **16** inhibits iron mobilization from BfrB in P. aeruginosa. Cells cultured in M63 media supplemented with 4 μM Fe were treated with analog **16** (125 μM) or with an equivalent volume of DMSO (control). (A) Enumerating viable cells shows that cultures treated with analog **16** (open circles) have approximately 2.5-fold fewer cells than untreated control (black circles) at all time points. (B) The iron stored in BfrB was visualized with the aid of native PAGE gels stained with Ferene S, which stains the iron stored in the interior cavity of BfrB blue. Recombinant BfrB (Rec. BfrB) was used to show the electrophoretic mobility of BfrB in the native PAGE gels. Lanes loaded with lysates of untreated control (DMSO) show iron stored in BfrB, with maximum accumulation in late exponential growth (ca. 15 h) and subsequent mobilization in the stationary phase. Lanes loaded with lysates of untreated control diluted 2-fold (0.5× DMSO) to account for the 2-fold larger number of viable cells in the untreated cultures show a similar trend. Lanes loaded with lysates of cells treated with **16** show significant inhibition of iron mobilization from BfrB. (C) Plot of peak areas obtained from densitometry analysis of the native PAGE gels in panel B. The open circles track the peak area in lanes loaded with lysates of cells treated with **16**, while the black circles track the peak area from the untreated control (0.5× DMSO). (D) Analysis of total iron levels normalized to viable cell count (CFU/mL) shows approximately 2-fold higher iron levels in cells treated with **16** (white bars), in agreement with nearly irreversible iron accumulation in BfrB. Error bars represent the standard deviation of three independent experiments. Panels B and C show results from a representative experiment.

can compensate for the absence of the iron storage protein. Nevertheless, the nearly independent growth defect observed in the first phase, which is in good agreement with the absence of BfrB, supports the idea that analogs **11** and **16** exhibit significant selectivity for BfrB in the P. aeruginosa cell. The sudden onset of toxicity observed in the second phase, which is not observed with the wild type cells, is probably related to off-target effects that expose a fitness vulnerability caused by the absence of BfrB. Consequently, it is possible to conclude that

the dose-dependent growth defect elicited by **11** or **16** on wild type P. aeruginosa cells is largely a consequence of the interaction between the small molecule inhibitors and BfrB in the bacterial cell. This issue was investigated in additional detail by probing the phenotypic and biochemical response of wild type cells treated with the small molecule inhibitors. The results of these studies are presented below.

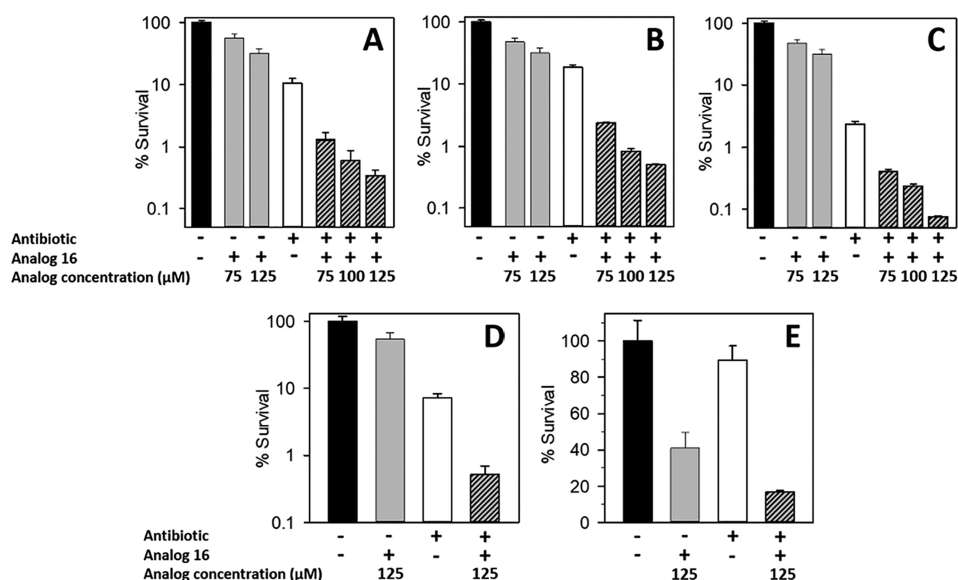**4-Aminoisoindoline-1,3-dione derivatives engage their target (BfrB) in P. aeruginosa cells.** Studies

Figure 9. Analog **16** potentiates the activity of fluoroquinolones. (A−C) *P. aeruginosa* PAO1 cultures in M63 media supplemented with 4 μM iron were treated with analog **16** only, fluoroquinolone at the reported MIC only, and a combination of analog **16** and fluoroquinolone at the MIC. The fluoroquinolones studied are (A) ciprofloxacin (0.25 μg/mL), (B) levofloxacin (0.5 μg/mL), and (C) norfloxacin (0.9 μg/mL). (D) *P. aeruginosa* clinical isolate MR3B cultures in M63 media supplemented with 4 μM iron were treated with analog **16** only, or ciprofloxacin only (0.2 μg/mL), or a combination of **16** and ciprofloxacin. (E) *P. aeruginosa* clinical isolate MR60 cultures in the same media as above were treated with analog **16**, or ciprofloxacin (1.0 μg/mL), or a combination of **16** and ciprofloxacin. Error bars represent the standard deviation from three independent experiments.

conducted to determine whether the analogs are capable of engaging BfrB and inhibiting iron mobilization from the bacterioferritin in the *P. aeruginosa* cytosol were conducted mainly with the most efficacious analog (**16**), and when practical, also with analog **11**, which is the most active of the two compounds harboring a −(CH$_2$)− linker. As indicated above, genetic manipulations were used in prior work to delete the *bfd* gene (Δbfd) and evaluate the consequences of inhibiting the BfrB−Bfd interaction in *P. aeruginosa*.[19] Preventing the BfrB−Bfd interaction in the Δbfd mutant cells dysregulates iron homeostasis by causing the irreversible accumulation of iron in BfrB and the concomitant depletion of free iron levels in the cytosol. The resultant phenotype is overproduction of the siderophore pyoverdin, which is ~4-fold larger than that secreted by wild type cells.[19] If the 4-aminoisoindoline-1,3-dione analogs are capable of binding BfrB, blocking the BfrB−Bfd interaction, and consequently inhibiting iron mobilization from BfrB in the *P. aeruginosa* cytosol, then they would be expected to elicit a similar pyoverdin hyper-production phenotype. To investigate whether 4-aminoisoindoline-1,3-dione derivatives indeed elicit such a phenotype, *P. aeruginosa* cells cultured in M63 media were treated with analog **16** at a concentration of 125 μM. As expected, cell cultures treated with the analog exhibited ca. 30% of viable cells relative to cells in the untreated control (Figure 7A). To analyze the levels of secreted pyoverdin, cells were pelleted and the supernatant was diluted 500-fold prior to measuring the fluorescence intensity at 455 nm (Figure 7B). Normalizing the intensity of pyoverdin fluorescence to cell density (CFU/mL) shows that cells treated with **16** secrete ~4-fold more pyoverdin than the untreated control (Figure 7C). To demonstrate that the intrinsic fluorescence of **16**, which is significantly weaker than that of pyoverdin, does not interfere with the measurement, the fluorescence spectrum from a solution of analog **16** (125 μM) after a 500-fold

dilution in PBS is shown in the green trace of Figure 7B. Similar observations are made when cell cultures are treated with analog **11** (Figure S6), albeit with a less pronounced phenotype, which is in agreement with the lower affinity of the analog for BfrB and correspondingly higher IC$_{50}$. These findings, which indicate that the analogs elicit the anticipated pyoverdin hyper-production phenotype in *P. aeruginosa*, suggest that they bind BfrB in the *P. aeruginosa* cytosol, block the BfrB−Bfd interaction, and inhibit iron mobilization from BfrB.

To obtain additional evidence that **16** blocks the BfrB−Bfd interaction and inhibits iron mobilization from BfrB in the *P. aeruginosa* cytosol, we resorted to visualizing BfrB-iron in native PAGE gels stained with Ferene S. A similar approach has been used to demonstrate that the Δbfd mutant irreversibly accumulates iron in BfrB.[19] To this end, cells cultured in M63 media supplemented with 4 μM iron were treated with **16** (125 μM) or with an equivalent volume of DMSO (control). At different time points cells were harvested by centrifugation after a small aliquot had been sampled to enumerate cell density (CFU/mL). The growth curves (Figure 8A) show that at every time point the number of viable cells in the untreated cultures is approximately 2.5-fold larger than in cultures treated with **16**. To visualize iron stored in BfrB, the cells harvested at different time points were lysed and the clarified supernatants were loaded onto native PAGE gels for separation and subsequent staining with Ferene S (Figure 8B); recombinant BfrB mineralized with an iron core of approximately 400 iron ions was used as a standard for the electrophoretic mobility of BfrB. Lanes loaded with lysate from untreated cells (DMSO) show that iron accumulating in BfrB reaches a maximum at *ca.* 15 h and then is mobilized. A similar trend is observed if the lysate solutions of untreated cells are diluted 2-fold prior to loading the gels (0.5× DMSO in Figure 8B), in order to account for the nearly 2-fold larger CFU/mL observed at each

time point relative to the treated culture. In contrast, the lanes loaded with lysates obtained from cultures treated with **16** show only iron accumulation in BfrB. The distinct trends of iron accumulation in BfrB observed with the treated vs untreated (0.5× DMSO) cultures can be readily visualized in the plot of Figure 8C, which was constructed with the aid of densitometry analysis of the gel bands. It is evident that the untreated cells store iron in BfrB during the logarithmic growth phase and then mobilize the stored reserves during the stationary phase. In contrast, when cells are treated with **16**, the flow of iron into BfrB appears to be mostly unidirectional, with much slower (inhibited) mobilization of iron from BfrB. Consistent with the nearly irreversible accumulation of iron in BfrB when cultures are treated with **16**, measurements of total cellular iron levels normalized to viable cell counts show that *P. aeruginosa* cells harbor approximately twice as much iron in the treated cultures relative to the untreated control (Figure 8D). Taken together, these observations strongly support the idea that blockade of the BfrB−Bfd interaction by **16** inhibits iron mobilization from BfrB and leads to nearly an irreversible accumulation of unusable iron in the bacterial cell.

4-Aminoisoindoline-1,3-dione derivatives enhance the killing activity of fluoroquinolones. Previous studies demonstrated that intact iron homeostasis is essential for bacterial cell survival under antibiotic stress, which suggests that bacterial iron homeostasis may be a potential target for boosting the action of antibiotics.[54,55] Consequently, we asked if the 4-aminoisoindoline-1,3-dione probes developed to disrupt bacterial iron homeostasis by blocking the BfrB−Bfd interaction would also potentiate the killing activity of antibiotics. The idea was initially tested by treating *P. aeruginosa* PAO1 cultures with (*i*) analog **16**, (*ii*) ciprofloxacin at the reported MIC[45] (0.25 μg/mL), and (*iii*) a combination of ciprofloxacin and analog **16**. The effect was evaluated 18 h post treatment by plating, enumerating viable cells (CFU/mL), and comparing the results to untreated cells (Figure 9A). Cultures treated with only analog **16** (125 μM) experienced the anticipated ∼30% survival, and cultures treated with only ciprofloxacin experienced approximately 10% survival relative to untreated control. In comparison, cultures treated with a combination of ciprofloxacin and analog **16** experienced significantly lower survival, in an analog-concentration depend-ent manner, such that when analog **16** was present at 125 μM the % survival was ∼50-fold lower relative to treatment with ciprofloxacin alone. Similar experiments carried out with the fluoroquinolones levofloxacin and norfloxacin revealed a similar enhancement of bactericidal activity, with approx-imately 50-fold lower cell survival of cultures treated with a combination of **16** (125 μM) and fluoroquinolone, relative to treatment with only the fluoroquinolone. Related experiments conducted with tobramycin and gentamycin (protein synthesis inhibitors) and with ceftazidime and imipenem (cell wall biosynthesis inhibitors) showed no enhancement of the antibacterial activity of these antibiotics when used in combination with the small molecule inhibitors of the BfrB−Bfd interaction (data not shown).

To extend these observations to include additional strains of *P. aeruginosa*, we conducted similar investigations with two cystic fibrosis clinical isolates (MR3B and MR60) obtained from Seattle Children's Research Foundation. Observations made with strain MR3B (Figure 9D) are similar to those made with strain PAO1 in that cultures of M3B treated with analog **16** (125 μM) experienced ca. 50% survival and cultures treated

with ciprofloxacin (0.2 μg/mL) experienced ca. 10% survival. In comparison, cultures treated with a combination of analog **16** and ciprofloxacin experienced 0.5% survival, or approx-imately 20-fold lower survival relative to treatment with ciprofloxacin alone. Strain MR60 is significantly more resistant to ciprofloxacin. When treated with ciprofloxacin at a concentration of 1 μg/mL, which is 4−5-fold higher than the dose used in experiments with strain PAO1 or MR3B, the MR60 strain experienced ca. 90% survival (Figure 9E). In comparison, MR60 cultures treated with analog **16** (125 μM) experienced ca. 40% survival and cultures treated with a combination of analog **16** and ciprofloxacin experienced ca. 10% survival, or approximately 4-fold lower survival relative to treatment with ciprofloxacin alone. These findings indicate that analogs of 4-aminoisoindoline-1,3-dione, such as analog **16**, have the potential for inhibiting the BfrB−Bfd interaction and enhance the activity of fluoroquinolones in a variety of *P. aeruginosa* strains.

■ DISCUSSION

Iron metabolism is emerging as an important unconventional target for the development of antibacterial strategies. The essentiality of iron for most pathogens, together with innate immune defenses which function to maintain very low concentrations of free iron *in vivo* ($\sim 10^{-20}$ M), present a formidable challenge to host colonization by pathogens and suggest that dysregulation of iron homeostasis constitutes a significant bacterial vulnerability. In agreement, gallium has been shown to disrupt bacterial iron metabolism,[56,57] and a recent report showed that systemic gallium treatment improves lung function in patients with chronic *P. aeruginosa* infection.[11] Ga^{3+}, which has an ionic radius similar to that of Fe^{3+}, is thought to perturb iron homeostasis by replacing Fe^{3+} in vital iron-utilizing proteins. Since Ga^{3+} cannot be reduced under physiological conditions, iron-utilizing proteins become inhibited, adversely affecting important metabolic paths. These observations, which underscore the significance of targeting iron metabolism as a viable approach to treat infections, also highlight the importance of developing rational means to dysregulate bacterial iron homeostasis to validate new targets and implement new strategies to develop novel antimicrobial therapies.

Previous investigations with *P. aeruginosa* showed that bacterial iron homeostasis can be perturbed by specifically interfering with the process of iron storage/mobilization from bacterioferritin.[19] Encouraged by these results we pursued a systematic, iterative strategy based on fragment screening, structural characterization of fragment binding, and synthetic elaboration of fragment hits to discover inhibitors of the BfrB−Bfd protein−protein interaction (Table 1). These small molecule analogs of 4-aminoisoindoline-1,3-dione selectively bind BfrB at the Bfd binding site and engage pockets on the BfrB surface where Y2 and L5 from Bfd anchor. X-ray crystallographic studies showed that all analogs in Table 1 bind at the Bfd-binding site on BfrB with nearly identical poses and interactions. These observations, which underscore the selectivity of the analogs for the Bfd-binding site on the BfrB surface, validate the structure-guided approach that led to their identification as inhibitors of the protein−protein interaction. The binding selectivity of the analogs for the Bfd binding site on BfrB endows analogs such as **16** with their ability to bind BfrB in the *P. aeruginosa* cytosol, perturb its interaction with Bfd, and inhibit the mobilization of BfrB-iron. Consequently,

the observations reported herein constitute proof of concept for the usefulness of chemical probes designed to perturb iron homeostasis by rationally interfering with a specific protein–protein interaction in the bacterial cell. Blockade of the BfrB–Bfd interaction with these chemical probes inhibits iron mobilization from BfrB and establishes a nearly unidirectional flow of iron into BfrB, which causes a significant fraction of the cellular iron to be "trapped" in BfrB and, therefore, accumulate as an unusable resource for the cell. The nearly irreversible accumulation of iron in BfrB is probably accompanied by a depletion of free iron in the cytosol, similar to that observed with the Δ*bfd* mutant,[19] which, as expected, is manifested in a pyoverdin hyperproduction phenotype. In this context, the growth defect elicited by the inhibitors is probably related to an intracellular iron limitation induced by blockade of the BfrB–Bfd interaction, which in turn is likely to exert an inhibitory effect on the biosynthesis and repair of iron-dependent enzymes that function in central physiological processes. Hence, the chemical probes reported herein provide a valuable starting point for future studies of structure–activity relationships that could lead to the identification of higher-affinity analogs as potential therapeutic lead compounds.

An important feature of utilizing chemical probes for dissecting biological systems is that these can be used alone, or in combination with other synergistic or antagonistic probes. Previous studies have shown that some antibiotics disrupt bacterial iron homeostasis and that the iron homeostasis machinery is important for bacterial cell survival in the presence of antibiotics.[54,58,59] Given that our results show that the inhibitors of the BfrB–Bfd interaction dysregulate iron homeostasis, we asked if the inhibitors would also boost the activity of antibiotics. This idea was tested initially with ciprofloxacin, and then with two other fluoroquinolones, norfloxacin and levofloxacin. The results show that the small molecule inhibitors of the BfrB–Bfd interaction boost the bactericidal activity of the fluoroquinolones approximately 50-fold. Additional work is clearly required to understand the reasons behind these observations. It is tempting, however, to speculate that the enhancement of the killing activity brought by the inhibitors of the BfrB–Bfd interaction may be related to the intracellular iron depletion caused by inhibiting the mobilization of iron from BfrB, which limits the pool of iron required to support the biogenesis or the repair of iron-dependent enzymes. In this context, it has been proposed that bactericidal antibiotics have well-established mechanisms of action, but that, in addition to these distinct mechanisms, subsequent metabolic changes such as elevated concentrations of TCA metabolites, active breakdown of the metabolic pool, and an elevated redox state also contribute to defining bactericidal activity.[60] It is therefore possible that the intracellular limitation of iron caused by inhibition of the BfrB–Bfd interaction impairs the biogenesis or the repair of important enzymes such as aconitase and succinate dehydrogenase of the TCA cycle, thus decreasing cell fitness and increasing the bacterial cell susceptibility to fluoroquinolone antibiotics. Consequently, it is possible to conceive a potential therapeutic strategy where inhibitors of the BfrB–Bfd interaction are used in combination with existing fluoroquinolone antibiotics.

■ ASSOCIATED CONTENT

ⓈSupporting Information

The Supporting Information is available free of charge on the ACS Publications website at DOI: 10.1021/jacs.9b00394.

> Figures S1–S6, crystallographic data (Table S1), synthetic procedures, fragment library screening using NMR spectroscopy, measurement of dissociation constants, and ^{1}H and ^{13}C spectra (PDF)

Accession Codes

Coordinates and structure factors were deposited to the Worldwide Protein Databank (www.wwPDB.org) with accession codes: Apo-BfrB (6NLF); C89S/K96C BfrB-fragment **1** (6NLG); BfrB-analog **11** (6NLI); Apo-BfrB-analog **12** (6NLJ); BfrB-analog **13** (6NLK); BfrB-analog **14** (6NLL); BfrB-analog **15** (6NLM); BfrB-analog **16** (6NLN).

■ AUTHOR INFORMATION

Corresponding Author

*mrivera@lsu.edu

ORCID Ⓞ

Blake R. Peterson: 0000-0001-8251-3579
Kevin P. Battaile: 0000-0003-0833-3259
Mario Rivera: 0000-0002-5692-5497

Present Address

▲Baskar Nammalwar: 10522 Parkdale Ave., San Diego, CA 92126. Krishna K. Gnanasekaran: 4591 Gatineau Ave., Mississauga, Ontario, Canada L4Z 2R9. Kate Eshelman: 10 Waterview Blvd., Parsippany, NJ 07054. Molly M. Lee: National Cancer Institute, Building 10, Hatfield CRC, Bethesda, MD 20892.

Author Contributions

●A.N.D.P.H. and H.Y. contributed equally.

Notes

The authors declare no competing financial interest.

■ REFERENCES

(1) CDC. Antibiotic Resistance Threats in the United States 2013. www.cdc.gov/drugresistance/threat-report-2013/.

(2) Blaskovich, M. A.; Butler, M. S.; Cooper, M. A. Polishing the tarnished silver bullet: the quest for new antibiotics. *Essays Biochem.* **2017**, *61* (1), 103–114.

(3) Laxminarayan, R.; Duse, A.; Wattal, C.; Zaidi, A. K.; Wertheim, H. F.; Sumpradit, N.; Vlieghe, E.; Hara, G. L.; Gould, I. M.; Goossens,

H.; Greko, C.; So, A. D.; Bigdeli, M.; Tomson, G.; Woodhouse, W.; Ombaka, E.; Peralta, A. Q.; Qamar, F. N.; Mir, F.; Kariuki, S.; Bhutta, Z. A.; Coates, A.; Bergstrom, R.; Wright, G. D.; Brown, E. D.; Cars, O. Antibiotic resistance-the need for global solutions. *Lancet Infect. Dis.* **2013**, *13* (12), 1057−98.

(4) Tacconelli, E.; Carrara, E.; Savoldi, A.; Harbarth, S.; Mendelson, M.; Monnet, D. L.; Pulcini, C.; Kahlmeter, G.; Kluytmans, J.; Carmeli, Y.; Ouellette, M.; Outterson, K.; Patel, J.; Cavaleri, M.; Cox, E. M.; Houchens, C. R.; Grayson, M. L.; Hansen, P.; Singh, N.; Theuretzbacher, U.; Magrini, N.; Group, W. H. O. P. P. L. W.. Discovery, research, and development of new antibiotics: the WHO priority list of antibiotic-resistant bacteria and tuberculosis. *Lancet Infect. Dis.* **2018**, *18* (3), 318−327.

(5) Burrows, L. L. The Therapeutic Pipeline for Pseudomonas aeruginosa Infections. *ACS Infect. Dis.* **2018**, *4* (7), 1041−1047.

(6) Boucher, H. W.; Talbot, G. H.; Bradley, J. S.; Edwards, J. E.; Gilbert, D.; Rice, L. B.; Scheld, M.; Spellberg, B.; Bartlett, J. Bad Bugs, No Drugs: No ESKAPE! An Update from the Infectious Diseases Society of America. *Clin. Infect. Dis.* **2009**, *48*, 1−11.

(7) Konstan, M. W.; Morgan, W. J.; Butler, S. M.; Pasta, D. J.; Craib, M. L.; Silva, S. J.; Stokes, D. C.; Wohl, M. E.; Wagener, J. S.; Regelmann, W. E.; Johnson, C. A. MBCHB for the Scientific Advisory Group and the Investigators and Coordinators of the Epidemiologic Study of Cystic Fibrosis, Risk factors for rate of decline in forced expiratory volume in one second in children and adolescents with cystic fibrosis. *J. Pediatr.* **2007**, *151* (2), 134−9.

(8) Crull, M. R.; Ramos, K. J.; Caldwell, E.; Mayer-Hamblett, N.; Aitken, M. L.; Goss, C. H. Change in Pseudomonas aeruginosa prevalence in cystic fibrosis adults over time. *BMC Pulm. Med.* **2016**, *16* (1), 176.

(9) Ballouche, M.; Cornelis, P.; Baysse, C. Iron Metabolism: A Promising Target for Antibacterial strategies. *Recent Pat. Anti-Infect. Drug Discovery* **2009**, *4*, 190−205.

(10) Foley, T. L.; Simeonov, A. Targeting iron assimilation to develop new antibacterials. *Expert Opin. Drug Discovery* **2012**, *7* (9), 831−47.

(11) Goss, C. H.; Kaneko, Y.; Khuu, L.; Anderson, G. D.; Ravishankar, S.; Aitken, M. L.; Lechtzin, N.; Zhou, G.; Czyz, D. M.; McLean, K. Gallium disrupts bacterial iron metabolism and has therapeutic effects in mice and humans with lung infections. *Sci. Transl. Med.* **2018**, *10* (460), No. eaat7520.

(12) Heinzl, G. A.; Huang, W.; Yu, W.; Giardina, B. J.; Zhou, Y.; MacKerell, A. D., Jr.; Wilks, A.; Xue, F. Iminoguanidines as Allosteric Inhibitors of the Iron-Regulated Heme Oxygenase (HemO) of Pseudomonas aeruginosa. *J. Med. Chem.* **2016**, *59* (14), 6929−42.

(13) Lueangsakulthai, J.; Jangpromma, N.; Temsiripong, T.; McKendrick, J. E.; Khunkitti, W.; Maddocks, S. E.; Klaynongsruang, S. A novel antibacterial peptide derived from Crocodylus siamensis haemoglobin hydrolysate induces membrane permeabilization causing iron dysregulation, oxidative stress and bacterial death. *J. Appl. Microbiol.* **2017**, *123* (4), 819−831.

(14) Cornelis, P.; Wei, Q.; Andrews, S. C.; Vinckx, T. Iron homeostasis and management of oxidative stress response in bacteria. *Metallomics* **2011**, *3* (6), 540−9.

(15) Bullen, J. J.; Rogers, H. J.; Spalding, P. B.; Ward, C. G. Iron and Infection: The Heart of the Matter. *FEMS Immunol. Med. Microbiol.* **2005**, *43*, 325−330.

(16) Weinberg, E. D. Iron Availability and Infection. *Biochim. Biophys. Acta, Gen. Subj.* **2009**, *1790*, 600−605.

(17) Hood, M. I.; Skaar, E. P. Nutritional immunity: transition metals at the pathogen-host interface. *Nat. Rev. Microbiol.* **2012**, *10* (8), 525−37.

(18) Benson, D. R.; Rivera, M. Heme Uptake and Metabolism in Bacteria. *Met. Ions Life Sci.* **2013**, *12*, 279−332.

(19) Eshelman, K.; Yao, H.; Punchi Hewage, A. N. D.; Deay, J. J.; Chandler, J. R.; Rivera, M. Inhibiting the BfrB:Bfd Interaction in *Pseudomonas aeruginosa* Causes Irreversible Iron Accumulation in Bacterioferritin and Iron Deficiency in the Bacterial Cell. *Metallocmics* **2017**, *9*, 646−659.

(20) Keyer, K.; Imlay, J. A. Superoxide Accelerates DNA-Damage by Elevating Free-Iron Levels. *Proc. Natl. Acad. Sci. U. S. A.* **1996**, *93*, 13635−13649.

(21) Rivera, M. Bacterioferritin: Structure Function and Protein-Protein Interactions. In *Handbook of Porphyrin Science*; Kadish, K. K., Smith, K. M., Guilard, R., Eds.; World Scientific Publishing: 2014; Vol. 30, pp 136−179.

(22) Andrews, S.; Norton, I.; Salunkhe, A. S.; Goodluck, H.; Aly, W. S.; Mourad-Agha, H.; Cornelis, P. Control of iron metabolism in bacteria. *Met. Ions Life Sci.* **2013**, *12*, 203−39.

(23) Rivera, M. Bacterioferritin: Structure, Dynamics and Protein-Protein Interactions at Play in Iron Storage and Mobilization. *Acc. Chem. Res.* **2017**, *50*, 331−340.

(24) Ruvinsky, A. M.; Vakser, I. A.; Rivera, M. Local packing modulates diversity of iron pathways and cooperative behavior in eukaryotic and prokaryotic ferritins. *J. Chem. Phys.* **2014**, *140* (11), 115104.

(25) Rui, H.; Rivera, M.; Im, W. Protein dynamics and ion traffic in bacterioferritin. *Biochemistry* **2012**, *51* (49), 9900−10.

(26) Yao, H.; Rui, H.; Kumar, R.; Eshelman, K.; Lovell, S.; Battaile, K. P.; Im, W.; Rivera, M. Concerted motions networking pores and distant ferroxidase centers enable bacterioferritin function and iron traffic. *Biochemistry* **2015**, *54* (8), 1611−27.

(27) Ma, J.-F.; Ochsner, U. A.; Klotz, M. G.; Nanayakkara, V. K.; Howell, M. L.; Johnson, Z.; Posey, J. E.; Vasil, M. L.; Monaco, J. J.; Hassett, D. J. Bacterioferritin A Modulates Catalase A (KatA) Activity and Resistance to Hydrogen Peroxide in *Pseudomonas aeruginosa*. *J. Bacteriol.* **1999**, *181*, 3730−3742.

(28) Weeratunga, S.; Lovell, S.; Yao, H.; Battaile, K. P.; Fischer, C. J.; Gee, C. E.; Rivera, M. Structural Studies of Bacterioferritin B (BfrB) from *Pseudomonas aeruginosa* Suggest a Gating Mechanism for Iron Uptake via the Ferroxidase Center. *Biochemistry* **2010**, *49*, 1160−1175.

(29) Weeratunga, S.; Gee, C. E.; Lovell, S.; Zeng, Y.; Woodin, C. L.; Rivera, M. Binding of *Pseudomonas aeruginosa* Apobacterioferritin-Associated Ferredoxin to Bacterioferritin B Promotes Heme Mediation of Electron Delivery and Mobilization of Core Mineral Iron. *Biochemistry* **2009**, *48*, 7420−7431.

(30) Yao, H.; Wang, Y.; Lovell, S.; Kumar, R.; Ruvinsky, A. M.; Battaile, K. P.; Vakser, I. A.; Rivera, M. The Structure of the BfrB-Bfd Complex Reveals Protein-Protein Interactions Enabling Iron Release from Bacterioferritin. *J. Am. Chem. Soc.* **2012**, *134* (32), 13470−81.

(31) Wang, Y.; Yao, H.; Cheng, Y.; Lovell, S.; Battaile, K. P.; Midaugh, C. R.; Rivera, M. Characterization of the Bacterioferritin/Bacterioferritin Associated Ferredoxin Potein-Protein Interactions in Solution and Determination of Binding Energy Hot Spots. *Biochemistry* **2015**, *54*, 6162−6175.

(32) Spring, D. R. Chemical genetics to chemical genomics: small molecules offer big insights. *Chem. Soc. Rev.* **2005**, *34* (6), 472−82.

(33) O'Connor, C. J.; Laraia, L.; Spring, D. R. Chemical genetics. *Chem. Soc. Rev.* **2011**, *40* (8), 4332−45.

(34) O'Toole, G. A.; Kolter, R. Initiation of biofilm formation in *Pseudomonas fluorescens* WCS365 proceeds via multiple, convergent signalling pathways: a genetic analysis. *Mol. Microbiol.* **1998**, *28* (3), 449−461.

(35) Chen, Y.; Wang, S.; Wang, S.; Liu, C.; Su, C.; Hageman, M.; Hussain, M.; Haskell, R.; Stefanski, K.; Qian, F. Initial Drug Dissolution from Amorphous Solid Dispersions Controlled by Polymer Dissolution and Drug-Polymer Interaction. *Pharm. Res.* **2016**, *33* (10), 2445−58.

(36) Kabsch, W. Automatic Indexing of Rotation Diffraction Patterns. *J. Appl. Crystallogr.* **1988**, *21*, 67−72.

(37) Vonrhein, C.; Flensburg, C.; Keller, P.; Sharff, A.; Smart, O.; Paciorek, W.; Womack, T.; Bricogne, G. Data Processing and Analysis with the AutoPROC Toolbox. *Acta Crystallogr., Sect. D: Biol. Crystallogr.* **2011**, *D67*, 293−302.

(38) Evans, P. R. An Introduction to Data Reduction: Space-Group Determination, scaling and intentisy statistics. *Acta Crystallogr., Sect. D: Biol. Crystallogr.* **2011**, *D67*, 282−292.

(39) McCoy, A. J.; Grosse-Kunstleve, R. W.; Adams, P. D.; Winn, M. D.; Storoni, L. C.; Read, R. J. Phaser crystallographic software. *J. Appl. Crystallogr.* **2007**, *40*, 658−674.

(40) Adams, P. D.; Afonine, P. V.; Brunkózci, G.; Chen, V. B.; Davis, I. W.; Echols, N.; Headd, J. J.; Hung, L.-W.; Kapral, G. J.; Grosse-Kunstleve, R. W.; McCoy, A. J.; Moriarty, N. W.; Oeffner, R.; Read, R. J.; Richardson, D. C.; Richardson, J. S.; Terwilliger, T. C.; Zwart, P. H. PHENIX: A Comprehensive Python-Based System for Macromolecular Structure Solution. *Acta Crystallogr., Sect. D: Biol. Crystallogr.* **2010**, *66*, 213−221.

(41) Emsley, P.; Lohkamp, B.; Scott, W. G.; Cowtan, K. Features and Development of Coot. *Acta Crystallogr., Sect. D: Biol. Crystallogr.* **2010**, *66*, 486−501.

(42) Liebschner, D.; Afonine, P. V.; Moriarty, N. W.; Poon, B. K.; Sobolev, O. V.; Terwilliger, T. C.; Adams, P. D. Polder maps: improving OMIT maps by excluding bulk solvent. *Acta Cryst. D* **2017**, *73* (2), 148−157.

(43) Chen, V. B.; Arendall, W. B. r.; Headd, J. J.; Keedy, D. A.; Immormino, R. M.; Kapral, G. J.; Murray, L. W.; Richardson, J. S.; Richardson, D. C. MolProbity: All-Atom Structure Validation for Macromolecular Crystallography. *Acta Crystallogr., Sect. D: Biol. Crystallogr.* **2010**, *66*, 12−21.

(44) McNicholas, S.; Potterton, E.; Wilson, K. S.; Noble, M. E. Presenting your Structures: The CCPmg Molecular-Graphics Software. *Acta Crystallogr., Sect. D: Biol. Crystallogr.* **2011**, *67*, 386−394.

(45) Andrews, J. M. Determination of Minimum Inhibitory Concentrations. *J. Antimicrob. Chemother.* **2001**, *48* (Suppl.1), 5−16.

(46) Sebaugh, J. L. Guidelines for accurate EC50/IC50 estimation. *Pharm. Stat* **2011**, *10* (2), 128−34.

(47) Chung, M. C. A specific iron stain for iron-binding proteins in polyacrylamide gels: application to transferrin and lactoferrin. *Anal. Biochem.* **1985**, *148* (2), 498−502.

(48) Abràmoff, M. D.; Magalhães, P. J.; Ram, S. J. Image processing with ImageJ. *Biophotonics International* **2004**, *11*, 36−42.

(49) Fish, W. W. Rapid colorimetric micromethod for the quantitation of complexed iron in biological samples. *Methods Enzymol.* **1988**, *158*, 357−64.

(50) Hennessy, D. J.; Reid, G. R.; Smith, F. E.; Thompson, S. L. Ferene—a new spectrophotometric reagent for iron. *Can. J. Chem.* **1984**, *62*, 721−724.

(51) Hedayati, M.; Abubaker-Sharif, B.; Khattab, M.; Razavi, A.; Mohammed, I.; Nejad, A.; Wabler, M.; Zhou, H.; Mihalic, J.; Gruettner, C.; DeWeese, T.; Ivkov, R. An optimized spectrophotometric assay for convenient and accurate quantitation of intracellular iron from iron oxide nanoparticles. *Int. J. Hyperthermia* **2018**, *34* (4), 373−381.

(52) Lepre, C. A.; Moore, J. M.; Peng, J. W. Theory and Applications of NMR-Based Screening in Pharmaceutical Research. *Chem. Rev.* **2004**, *104*, 3641−3675.

(53) Wijerathne, H.; Yao, H.; Wang, Y.; Lovell, S.; Battaile, K. P.; Rivera, M. Bfd, a New Class of [2Fe-2S] Protein That Functions in Bacterial Iron Homeostasis, Requires a Structural Anion Binding Site. *Biochemistry* **2018**, *57*, 5533−5543.

(54) Yeom, J.; Imlay, J. A.; Park, W. Iron homeostasis affects antibiotic-mediated cell death in Pseudomonas species. *J. Biol. Chem.* **2010**, *285* (29), 22689−95.

(55) Mehi, O.; Bogos, B.; Csorgo, B.; Pal, F.; Nyerges, A.; Papp, B.; Pal, C. Perturbation of iron homeostasis promotes the evolution of antibiotic resistance. *Mol. Biol. Evol.* **2014**, *31* (10), 2793−804.

(56) Kaneko, Y.; Thoendel, M.; Olakanmi, O.; Britigan, B. E.; Singh, P. K. The Transition Metal Gallium Disrupts *Pseudomonas aeruginosa* Iron Metabolism and has Antimicrobial and Antibiofilm Activity. *J. Clin. Invest.* **2007**, *117*, 877−887.

(57) Minandri, F.; Bonchi, C.; Frangipani, E.; Imperi, F.; Visca, P. Promises and failures of gallium as an antibacterial agent. *Future Microbiol.* **2014**, *9* (3), 379−97.

(58) Dwyer, D. J.; Belenky, P. A.; Yang, J. H.; MacDonald, I. C.; Martell, J. D.; Takahashi, N.; Chan, C. T.; Lobritz, M. A.; Braff, D.;

Schwarz, E. G.; Ye, J. D.; Pati, M.; Vercruysse, M.; Ralifo, P. S.; Allison, K. R.; Khalil, A. S.; Ting, A. Y.; Walker, G. C.; Collins, J. J. Antibiotics induce redox-related physiological alterations as part of their lethality. *Proc. Natl. Acad. Sci. U. S. A.* **2014**, *111* (20), E2100−9.

(59) Dwyer, D. J.; Kohanski, M. A.; Hayete, B.; Collins, J. J. Gyrase inhibitors induce an oxidative damage cellular death pathway in *Escherichia coli*. *Mol. Syst. Biol.* **2007**, *3*, 91.

(60) Belenky, P.; Ye, J. D.; Porter, C. B. M.; Cohen, N. R.; Lobritz, M. A.; Ferrante, T.; Jain, S.; Korry, B. J.; Schwarz, E. G.; Walker, G. C.; Collins, J. J. Bactericidal Antibiotics Induce Toxic Metabolic Perturbations. *Cell Rep.* **2015**, *13*, 968−980.